

Cite this: *RSC Advances*, 2012, 2, 4844–4856

www.rsc.org/advances

PAPER

Looped carbon capturing and environmental remediation: case study of magnetic polypropylene nanocomposites†

Jiahua Zhu,^{ab} Hongbo Gu,^a Sowjanya B. Rapole,^{ab} Zhiping Luo,^c Sameer Pallavkar,^a Neel Haldolaarachchige,^d Tracy J. Benson,^a Thomas C. Ho,^a Jack Hopper,^a David P. Young,^d Suying Wei^{*b} and Zhanhu Guo^{*a}

Received 21st November 2011, Accepted 21st March 2012

DOI: 10.1039/c2ra01150f

A waste-free process to recycle Fe@Fe₂O₃/polypropylene (PP) polymer nanocomposites (PNCs) is introduced to synthesize magnetic carbon nanocomposites (MCNCs) and simultaneously produce useful chemical species which can be utilized as a feedstock in petrochemical industry. The magnetic nanoparticles (NPs) are found to have an effective catalytic activity on the pyrolysis of PP. The PNCs (with a NP loading of 20.0 wt%) undergo a complete degradation with 2 h pyrolysis at 500 °C in a H₂/Ar atmosphere and the degradation components exhibit a distribution of species with different numbers of carbon, while only 40% of pure PP is decomposed after applying the same pyrolytic conditions. The coked solid waste from the conventional process has been utilized as a carbon source to form a protective carbon shell surrounding the magnetic NPs. The magnetic carbon nanocomposites (MCNCs) pyrolyzed from PNCs containing 20.0 wt% NPs demonstrate extremely fast Cr(VI) removal from wastewater with the almost complete removal of Cr(VI) within 10 min. The pH effect on the Cr(VI) removal efficiency is investigated with a preferable value of 1–3. The adsorbent exhibits much higher adsorption capacity in acidic solutions than that in alkali solutions. The large saturation magnetization (32.5 emu g⁻¹) of these novel magnetic carbon nanocomposites allows fast recycling of both the adsorbents and the adsorbed Cr(VI) from the liquid suspension in a more energetically and economically sustainable way by simply applying a permanent magnet. The significantly reduced treatment time required to remove the Cr(VI) makes these MCNCs promising for the efficient removal of the heavy metals from wastewater. Kinetic investigation reveals the pseudo-second-order adsorption of Cr(VI) on these novel magnetic carbon nanocomposite adsorbents.

1. Introduction

The ever increasing disposal of municipal solid waste (MSW) has placed serious environmental problems in the last few decades. The amount of MSW generated in the United States continues to increase, from each person 2.68 lb day⁻¹ in 1960 to each person 4.34 lb day⁻¹ in 2009.¹ The total MSW generation was as high as 243 million tons in 2009 and new technologies to recycle MSW in a more efficient and sustainable manner are in great demand. From the United States Environmental Protection Agency (EPA) report, the recycling rate of the MSW has increased significantly

from 6.4% in 1960 to 33.8% in 2009.¹ However, much more effort is still required to recycle plastics due to the very low recycled amount for some types of plastic wastes. For instance, polypropylene (PP) accounted for 13.6% of the total plastic waste in the United States in 2000 and only about 0.3% was recycled.¹

Land-filling, incineration and recycling are currently the major options for MSW treatment.^{2,3} However, landfill has environmental risks due to the chemical inertness of the plastics and limited available space, which is another drawback of this method. Incineration, not widely used primarily because of the potential generation of toxic gaseous products and ash, only shifts a solid waste issue to an air pollution problem. Recycling plastic waste obtains great benefits in terms of the environmental concerns and economic feasibility, which includes reducing the need for landfilling and incineration, preventing the pollution caused by the manufacturing of products from raw materials, decreasing the emissions of greenhouse gases, and conserving the natural resources such as timber, water, and minerals. The options for plastic recycling are divided into four major groups: (1) reusing the plastics directly for other applications; (2) reprocessing waste plastics to secondary products; (3) recovering

^aIntegrated Composites Laboratory (ICL), Dan F. Smith Department of Chemical Engineering, Lamar University, Beaumont, TX 77710, USA. E-mail: zhanhu.guo@lamar.edu; Tel: (409) 880-7654 (Z. G.)

^bDepartment of Chemistry and Biochemistry, Lamar University, Beaumont, TX 77710, USA. E-mail: suying.wei@lamar.edu; Tel: (409) 880-7654 (S.W.)

^cMicroscopy and Imaging Center and Materials Science and Engineering Program, Texas A&M University, College Station, TX 77843, USA

^dDepartment of Physics and Astronomy, Louisiana State University, Baton Rouge, LA 70803, USA

† Electronic supplementary information (ESI) available. See DOI: 10.1039/c2ra01150f

valuable chemical resources from waste plastics; (4) incinerating waste plastics to recover energy.⁴ Pyrolysis is an attractive resource recovery approach that converts plastic waste to valuable chemicals and/or monomers to produce new polymers. Compared to thermal pyrolysis, catalytic pyrolysis is preferred to improve the yield of valuable products, lower the reaction temperature, increase the yield of gasoline (C₅–C₁₂) and/or alter the composition of the oil product.⁵ Acidic catalysts (zeolites ZSM-5, moedenite, zeolite-Y, and a sulfur-promoted zirconia),⁶ base promoted iron catalysts supported on γ -alumina,⁷ zeolite and clay based microporous catalysts,⁸ and even enzyme (*Candida antarctica* lipase)³ were used in recycling the different types of polymer waste to improve the yield and to enhance the selectivity of the products. However, catalyst deactivation by poisoning, fouling and thermal degradation is of a great concern in the catalytic processes due to the huge cost for the catalyst replacement and process shutdown.

With the rapid development of novel multifunctional polymer nanocomposites (PNCs), unique physicochemical properties have been revealed and tremendous potential applications have been discovered deriving from these novel nanostructured materials.^{9–18} For examples, poly(vinylidene fluoride-co-hexafluoro propylene) nanocomposites reinforced with surface modified BaTiO₃ nanoparticles (NPs) have demonstrated the capacity to sustain high energy density¹⁹ and β -MnO₂/polypyrrole nanorod composites have served as high performance supercapacitors with a specific capacitance of 294 F g⁻¹.²⁰ Moreover, these various newly designed and fabricated PNCs have shown great applications such as in electronics, like light-emitting diode (LED),²¹ electrocatalysts in fuel cell systems,²² strain sensors,²³ and microwave absorbers.^{24,25} Be aware of the current challenges in recycling the plastic waste, how to efficiently recycle PNCs becomes even much more challenging due to the complex components and unpredictable degradation species with the existence of the nanofillers. Especially, PNCs filled with 3d transition metals such as Fe, Co, and Ni NPs,^{7,26–28} the pyrolysis pathway of the PNCs can be significantly different from that of the pure polymers.²⁸ Meanwhile, the strong affinity of the polymers with the particle surfaces inevitably generates more coke to deactivate the catalysts in the pyrolysis process. Ways to comprehensively and sustainably recycle the PNCs for valuable products are demanded for academic understanding and industrial applications; however they are rarely studied.

3d transition metal including Fe, Co and Ni NPs are of great interest due to their unique magnetic properties and catalytic activity.^{24,29–38} However, these bare metal particles especially in the nanoscale are readily oxidized or even ignite spontaneously upon exposure to air.^{38–40} Therefore, a protecting shell structure is often introduced to extend the applications of these NPs.⁴¹ Typically, these protective shells including silica,^{39,41,42} polymer,⁴³ carbon^{44,45} and noble metals.^{46,47} Compared to other shells, the carbon shell with much higher stability in harsh environments⁴⁸ and large specific surface area has shown an enhanced efficiency in the wastewater treatment.⁴⁵ The reported techniques to synthesize carbon shells include magnetron and ion-beam co-sputtering,⁴⁹ high temperature annealing,⁵⁰ catalytic chemical vapor deposition,⁵¹ and pyrolysis of organometallic compounds⁵² or polymers.^{32,40} However, all these methods are costly, which limits their large-scale application. An economic method for large-scale synthesis of carbon coated metallic NPs is

still not available. These carbon-coated magnetic NPs have been demonstrated as effective adsorbents for Cr(VI) removal from wastewater with great advantages of high adsorption capacity and facile recycling by simply using a permanent magnet^{45,53} as compared to the conventional adsorbents such as activated carbon,^{54,55} biomass⁵⁶ and Fe(III)/Cr(III) hydroxides.⁵⁷ A recent review reporting on the synthesis and versatile applications of magnetic carbon nanocomposites (MCNCs) reveals the great advantages of these materials.⁵⁸ However, different from the traditional method which includes intentionally introducing a polymer layer on the nanoparticle surface and then converting it to carbon, the carbon source from the recycled PNCs is simultaneously used to produce the MCNCs for heavy metal removal has been rarely studied so far.

In this paper, a comprehensive and sustainable waste-free coupled process of polymer nanocomposite (PNC) recycling is introduced to synthesize magnetic carbon nanocomposites (MCNCs) and to produce useful chemical radicals simultaneously. Briefly, Fe@Fe₂O₃/PP PNCs are fabricated using a facile organometallic thermal decomposition method. Following by a pyrolysis process under H₂ (5%)/Ar environment at 500 °C for 2 h, the embedded NPs serve as catalysts for the PP pyrolysis. The coke produced on the NP surface during heating serves as a carbon source for the *in situ* formation of a carbon shell structure and the volatile phase is collected as a useful chemical resource or potential liquid fuel upon condensation. The related products have been thoroughly analyzed. The gas and polymer gel components are analyzed by the gas chromatography/mass spectrometry (GC-MS). The mechanisms of PP pyrolysis with and without NPs are comparatively proposed and discussed. The MCNCs are characterized by high resolution transmission electron microscopy (HRTEM), X-ray diffraction (XRD), thermogravimetric analysis (TGA) and magnetic measurements. Meanwhile, the feasibility of these MCNCs serving as novel adsorbents to remove Cr(VI) from wastewater is tested and the results show that the MCNCs have a large adsorption capacity and high removal efficiency. The adsorption kinetics and solution pH dependent adsorption behaviour are also detailed in this work.

2. Experimental

2.1. Materials

The isotactic PP used in this study was supplied by Total Petrochemicals Inc. USA (0.9 g cm⁻³ in density, $M_n \approx 40\,500$, $M_w \approx 155\,000$, melt index ≈ 35 g min⁻¹). Iron(0) pentacarbonyl (iron carbonyl, Fe(CO)₅, 99%) and three alkene standard chemicals of 1-tridecene (C₁₃₌, 96%), 1-hexadecene (C₁₆₌, > 99%) and 1-nonadecene (C₁₉₌, > 99%) were commercially obtained from Sigma Aldrich. Potassium dichromate (K₂Cr₂O₇, 99%) and 1,5-diphenyl carbazide (DPC) were purchased from Alfa Aesar. *o*-Phosphoric acid (H₃PO₄, 85 wt%) and xylene (laboratory grade, $\rho = 0.87$ g cm⁻³) were purchased from Fisher Scientific. All the chemicals were used as received without further treatment.

2.2 Fabrication of polymer nanocomposites and the pyrolysis process

The PP nanocomposites were prepared following the reported procedures.³¹ Briefly, PP was initially dissolved in xylene with a

weight ratio of 1 : 10 (20 g : 207 mL) and refluxed at the boiling point (~ 140 °C) of xylene for around 2 h until the PP was completely dissolved. Then different weights (2.17 and 17.48 g) of $\text{Fe}(\text{CO})_5$ were injected into the dissolved PP dispersion to obtain the final PNCs containing 3.0 and 20.0 wt% of the NPs (based on pure elemental iron). The mixture solution turned from transparent to yellow immediately after the addition of $\text{Fe}(\text{CO})_5$ and then gradually changed to black during the additional 3 h refluxing process under nitrogen protecting conditions, indicating the formation of the NPs. Upon heating, $\text{Fe}(\text{CO})_5$ decomposed to $\text{Fe}_2(\text{CO})_9$ and $\text{Fe}_3(\text{CO})_{12}$ with the rapid formation of CO, reaching an equilibrium mixture of all the three carbonyls. The $\text{Fe}_3(\text{CO})_{12}$ was then decomposed and finally formed the metallic NPs.^{59,60} The PNC solution was then cooled to around 90 °C and poured onto a large glass plate to allow solvent evaporation overnight. After that, the solid residues (powder-like products) were collected and dried in a vacuum oven at room temperature overnight.

To recycle the PNC waste, the PNCs were placed in a horizontal quartz tube and heated to 500 °C with a heating rate of 10 °C min^{-1} under the gas atmosphere of $\text{H}_2(5\%)/\text{Ar}$. The effect of the particle loading was also investigated by using PNCs with a particle loading of 3.0 and 20.0 wt%. The samples were denoted S3 and S20, respectively. The gas components, polymer gel components and solid particles decomposed from S3/S20, denoted SG3/SG20, SS3/SS20 and SP3/SP20, were collected for analysis. The schematic process for the polymer nanocomposite preparation and its thermal decomposition to various products is shown in Scheme 1. The gas samples were collected using Tedlar bag (SKC Inc., Part No. 232-05) from the downstream of the quartz tube 5 min later once the temperature reaches 500 °C. The polymer gels were condensed at the end of the quartz tube and they were scraped from the tube for further analysis after the heating process.

2.3 Characterization

GC-MS for gas component analysis. The collected gas samples were diluted by nitrogen gas (ultrahigh purity grade, Airgas) in a Tedlar bag (SKC Inc., Part No. 232-05) with a dilution factor of 5000. The analytical tool used for the gas sample analysis was a gas chromatograph/mass spectrometer system (Varian CP-3800/Saturn 2200) with a built-in cryo-focus trap unit designed by Lotus Consulting Agency, to achieve a detection capability in the parts per billion (ppb) range. Liquid nitrogen was used as the refrigerant to freeze the sample in the cryo-focus trap unit during

the pre-concentration stage, with He (ultra high purity grade, Airgas) as the purge gas.

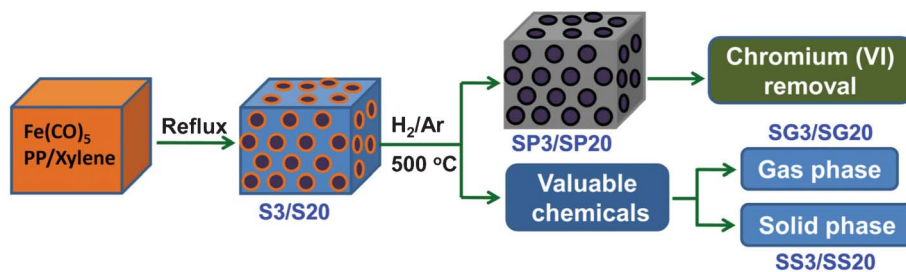
GC-MS for polymer gel analysis. A Varian CP-3800 gas chromatograph (GC) equipped with a Saturn 2000 ion trap mass spectrometer (MS) was used for identification and quantitation of the degraded polypropylene samples (polymer gels were samples diluted by toluene with 1/40 weight ratio before analysis). The chromatographic column used was an Rxi-1 ms (30 m \times 0.52 mm, 0.25 μm film thickness), purchased from Restek, Inc. (Bellefonte, PA, USA). The temperature profile for the GC oven started at 50 °C, held for 2 min, ramped at 10 °C min^{-1} to 320 °C, and finally held for 2 min. Both electron impact ionization (EI, sample is vaporized into the mass spectrometer ion source and impacted by a beam of electrons with sufficient energy to ionize the molecule) and chemical ionization (CI, molecules introduced to EI source at high pressure generate ion types of $[\text{M} + \text{R}]^+$ rather than conventional M^+ molecule ion) techniques were employed for compound identification. Acetonitrile was used as the CI reagent gas, which yielded the $[\text{M} + 40]$ (M indicates the molecular weight of the species to be determined, 40 is the molecular weight of the acetonitrile ion) ions for molecular mass determination.

The thermal degradation of the decomposed polymer gels was studied with a thermobalance (TA instruments TGA Q-500) from 25 to 550 °C in nitrogen atmosphere, with a flow rate of 60 mL min^{-1} and a heating rate of 10 °C min^{-1} . The carbon-coated NPs (SP3/SP20) were analyzed in an air atmosphere from 25 to 775 °C with the same flow rate and heating rate.

The morphology of the carbon-coated SP3/SP20 NPs was determined using a FEI Tecnai G² F20 microscope with field emission gun, operated at an accelerating voltage of 200 kV. Samples for TEM observation were prepared by drying a drop of SP3/SP20-ethanol suspension on the carbon-coated copper TEM grids.

The powder X-ray diffraction analysis of the SP3/SP20 was carried out with a Bruker AXS D8 Discover diffractometer with GADDS (General Area Detector Diffraction System) operating with a $\text{Cu-K}\alpha$ radiation source filtered with a graphite monochromator ($\lambda = 1.5406$ Å).

For the magnetic measurements, a plastic drinking straw was used as the sample holder. A small portion of each sample, approximately 5–10 mg, was loaded into the straw. The magnetic moment of the sample was measured at room temperature in a commercial magnetometer (Quantum Design PPMS system),



Scheme 1 The schematic process for the polymer nanocomposite preparation, thermal decomposition and application of the decomposed products. S3 and S20 indicate the polymer nanocomposites (PNCs) with a nanoparticle loading of 3.0 and 20.0 wt%. SG3/SG20, SS3/SS20 and SP3/SP20 represent the gas phase components, polymer gel components and solid particles decomposed from S3/S20, respectively.

which is a Faraday-extraction type magnetometer. At each field value, 10 scans were measured and averaged.

Chromium removal. The effects of the adsorbent (SP20) and the dichromate concentration on the Cr(VI) removal percentage (%) were studied. Cr(VI) solutions with different concentrations (0.4, 0.8, 1.0, 1.2 and 1.5 mg L⁻¹ in DI water) were treated with 1.0 g L⁻¹ SP20 to study the adsorption capacity. For adsorbent concentration study, the potassium dichromate solution containing 1.5 mg L⁻¹ Cr(VI) was treated with different concentrations of SP20 NPs (0.5, 1.0, 1.5, 2.0 and 2.5 g L⁻¹). Briefly, the mixture was kept under ultrasonication at room temperature for 10 min. Then, the SP20 NPs were separated from the solutions by centrifuging (Fisher Scientific, Centrifuge 228). Meanwhile, SP20 can be separated from the solutions by using a permanent magnet and gave similar analytical results. The clear solutions were then collected and subjected to colorimetric analysis to determine the remaining chromium concentrations. For the kinetic study, the SP20 concentration was kept at 1 g L⁻¹ in the neutral solution for different adsorption times such as 10, 20, 30, 60 and 120 min. The pH study was conducted at different pH values from 1 to 11, the pH value was adjusted by using hydrochloric acid (using 1 mol L⁻¹ HCl to adjust pH from pH 2–4 and concentrated HCl for pH = 1) or sodium hydroxide solutions (1 mol L⁻¹). For colorimetric analysis,⁶¹ the aforementioned clear solutions (5.25 mL) were taken into test tubes, *o*-phosphoric acid (0.50 mL, 4.5 M) and DPC (0.25 mL, 5 g L⁻¹) were added. After incubation at room temperature for 30 min for color development, the absorbance of the samples was measured in a UV-vis spectrophotometer (Cary 50). Peaks with varied intensities were observed in the spectrometer scans at 540 nm wavelength depending on the concentrations of the remaining Cr(VI) in the samples.

3. Results and discussion

3.1 Gas components

Pure PP and S3/S20 PNCs were processed following the same pyrolysis procedures. The gas component and polymer gel component were collected separately during pyrolysis and were analyzed by GC-MS in order to identify the chemical structure of the evolved products. The GC traces for the gas products are shown in Fig. 1 and the assigned structure for each peak is displayed in Table 1. The species of the gas component consist of mainly three categories: alkanes, alkenes and aromatic compounds (No. 15 in Table 1). This product distribution is slightly different from previous literature reports where dienes were often observed.^{4,62} The structures were identified through the analysis of the mass fragmentation patterns as compared to the standard patterns of the pure chemical compounds. Most of the gas compounds obtained from both pure PP and S3/S20 PNCs are observed to be the same with a slight difference in the fraction, Table 1. For example, the major species of the gas component numbered 1, 2, 3, 4 and 7, representing 2,5-dimethyl-3-hexene (*m/z* 112), 3,4-diethyl-3-hexene (*m/z* 140), 3-methyl-1-butene (*m/z* 70), 1-pentene (*m/z* 70) and 2,4-dimethyl-hexane (*m/z* 114), respectively, are observed in all the three samples in considerable fraction.

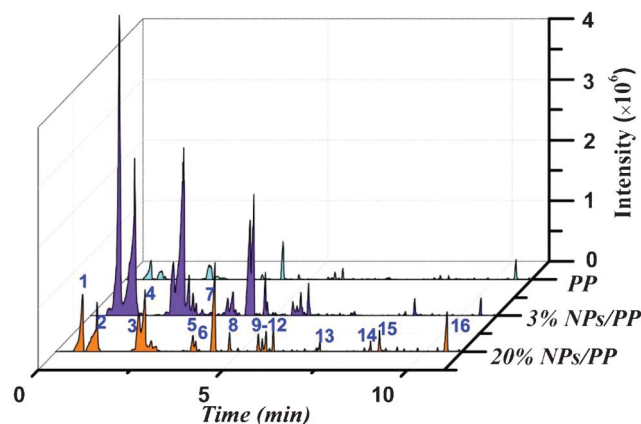


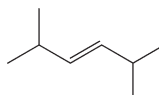
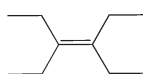
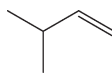
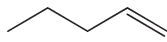
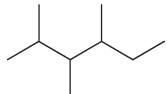
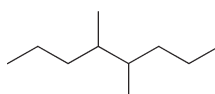
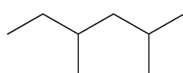
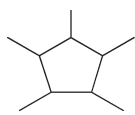
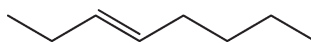
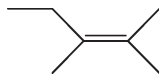
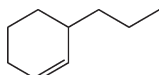
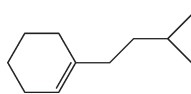
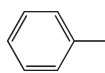
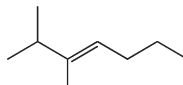
Fig. 1 GC spectra of the gas components pyrolyzed from pure PP and NPs/PP PNCs.

The pyrolysis pathway that leads to the observed major products with different carbon numbers is clarified in Scheme 2 based on the reaction types proposed by Tsuchiya *et al.*⁶³ The degradation is initiated by the random scission on the PP chains and thus primary (p) and secondary radicals (s) are formed. These free radicals either go further to abstract hydrogen from the long PP chains to form a tertiary (t) radical or recombine with free radicals to form alkanes. Generally, the alkenes are formed by radical transfer followed by a β -scission to generate a double bond, such as product no. 3. The formation of products no. 1 and 2 is more complex, that involves a radical attraction to a small alkene molecule and then forms larger radicals. These larger radicals follow a radical transfer (from primary to secondary/tertiary radical) and β -scission to form alkene (product no. 1) or radical–radical recombination to form a new double bond (product no. 2 and no. 4). The alkanes (product no. 7) are formed by four major steps—random scission, radical transfer, β -scission and hydrogenation. Although other steps that not explicitly drawn here are possible for the other products, the formation of these dominant products suggests that the pyrolysis mechanism in Scheme 2 represents the major reaction pathways.

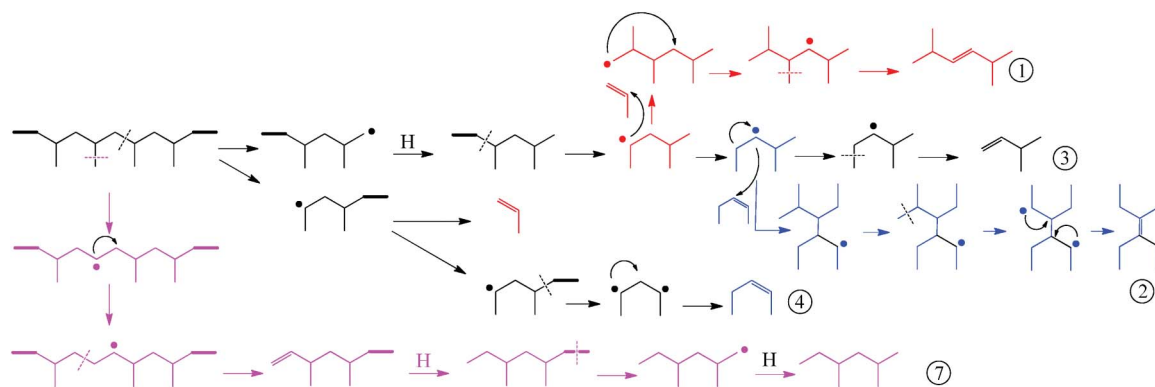
3.2 Polymer gel components

Fig. 2 shows the typical GC traces of the diluted polymer gel (SS3) pyrolyzed from S3 PNCs. Pure PP and SS20 give similar GC peaks following the same analysis procedure, Fig. S1† and S2†. EI mass spectra data, insets (I) and (II) in Fig. 2, present the molecular weight information. Analysis of the chromatograms showed distinct groupings of peaks along the retention time axis. Decomposition components are identified using mass spectrometry according to the molecular weight and structural type, which are further verified by matching the retention time with those using standard compounds from Sigma-Aldrich. The EI results indicate that all the detected compounds have similar but different structures. Analysis of the CI results (Fig. S3†) on each peak of different retention times from the EI chromatograms, Fig. 2, show the same molecular mass within each of the groupings. Therefore, it was concluded that the compounds within the same group were isomers. For verification, available standards (C₁₃₌, C₁₆₌ and C₁₉₌) were purchased and analyzed.

Table 1 Gas products of pure PP and its NPs/PP PNCs

Species (no.)	<i>m/z</i>	Fraction (%)			Structures
		PP	3.0 wt% NPs	20.0 wt% NPs	
1	112	14.81	23.42	12.29	
2	140	8.45	18.47	12.73	
3	70	15.34	5.02	9.56	
4	70	4.3	19.27	12.40	
5	128	2.64	0.97	2.36	
6	142	<i>μ</i>	2.01	1.17	
7	114	15.05	13.86	14.62	
8	140	1.39	1.67	1.85	
9	82	1.05	0.75	1.86	
10	112	/	0.42	1.22	
11	98	2.94	1.24	2.14	
12	124	2.96	1.20	2.00	
13	152	1.30	/	0.97	
14	196	1.21	/	0.96	
15	92	0.83	0.62	2.23	
16	126	6.40	0.57	4.64	
Others		21.33	10.51	17.00	

^a “/” indicates the component, which is not available in the products.



Scheme 2 The degradation mechanism for the major gas components.

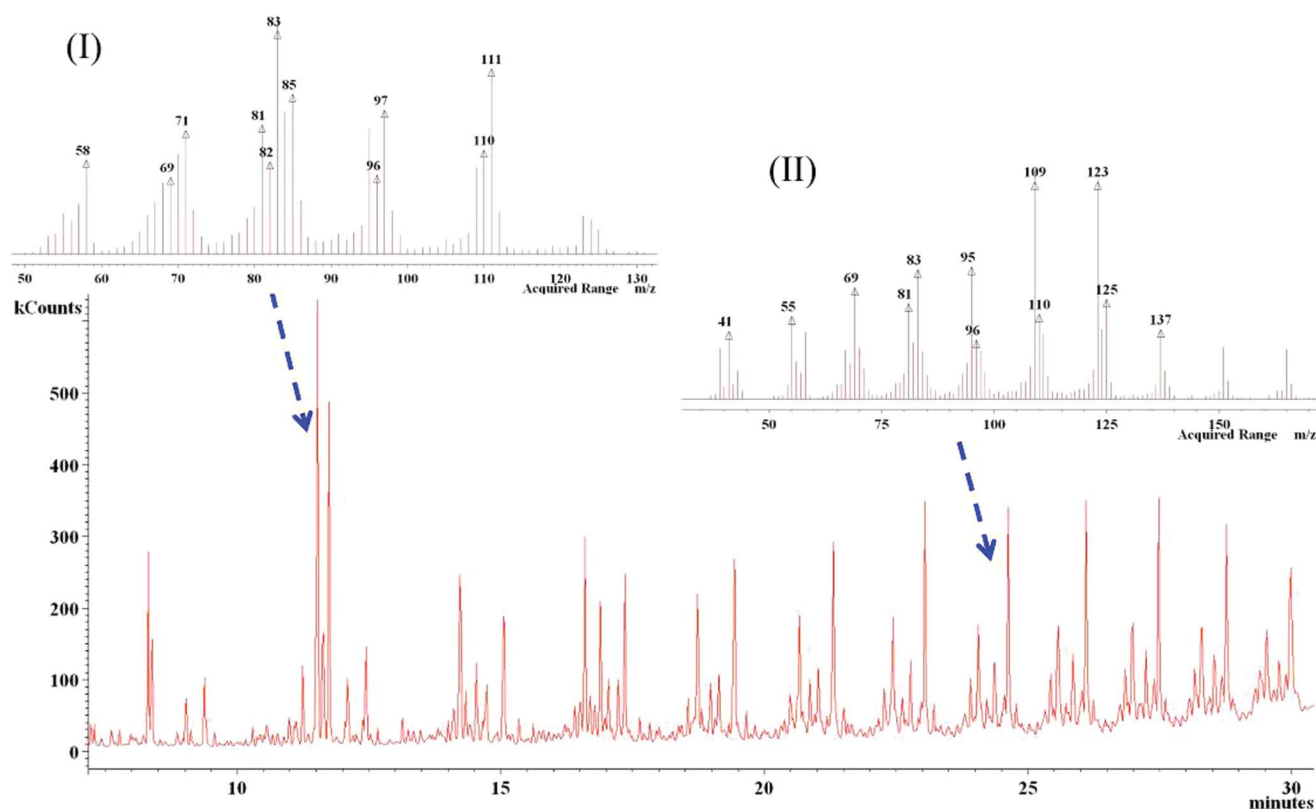


Fig. 2 Typical GC-MS ion chromatogram for the polymer gel after pyrolysis of the S3 PNCs. Inset figures (I) and (II) are the EI mass spectra data presenting the molecular weight information. The polymer gel was diluted by toluene with 1/40 weight ratio before analysis. Similar spectra were obtained from pure PP and S20 PNCs.

Quantitation was based upon the $C_{13=}$ standard for the C_{13} peaks, $C_{16=}$ standard for the C_{16} peaks, and $C_{19=}$ standard for all remaining peaks, all using EI mode. As one can see, there are peaks up to C_{43} , Fig. 3. Standards beyond the C_{19} were not available; however, in terms of retention times and mass spectra, these peaks are consistent with the smaller molecular weight species that elute earlier from the GC column.

Fig. 3 shows the product yields of the polymer gel from pure PP and S3/S20 PNCs. By analyzing the concentration of each component with different carbon numbers from C_{13} to C_{43} , it is evident that SS3 and SS20 are able to generate more low carbon number molecules than SS(PP). The concentration of each

component increases significantly after introducing 3% NPs into the PP matrix. Typically, the concentration of C_{19} in SS3 is 2.38 mg mL^{-1} , which is 145% higher than that of 0.97 mg mL^{-1} of pure PP. SS3 exhibits the highest concentration of lower carbon number species (C_{13} – C_{19}), while the highest concentration of C_{22} – C_{43} is dominated by SS20. In particular, the yield products of SS20 from C_{25} to C_{43} are nearly doubled as compared to those of pure PP. These results indicate that the thermal decomposition of PP could be significantly affected by the existence of small amount of Fe@Fe₂O₃ NPs. The large difference in the fraction of various species arises from the catalytic activity of the embedded NPs, which have been

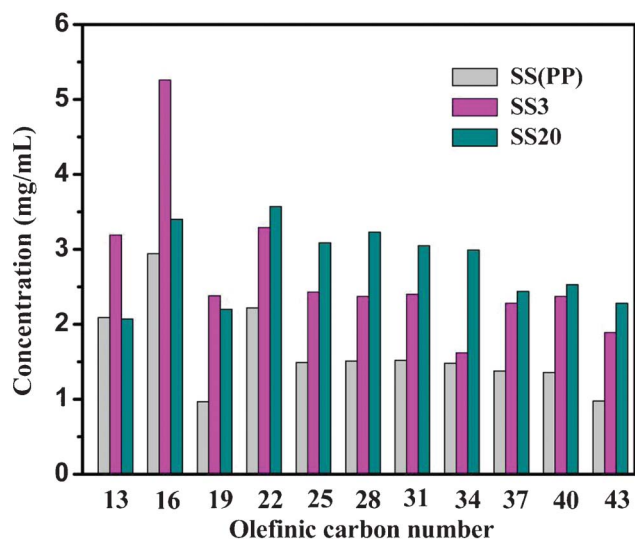


Fig. 3 Product yield of the polymer gel pyrolysis components from PP and PNCs. ($\text{H}_2(5\%)/\text{Ar}$ gas, $500\text{ }^\circ\text{C}$, 2 h). Compounds were identified using EI and CI methods, and by retention times from standard compounds. SS(PP) represents the collected polymer gel components after thermal decomposition of pure PP. The samples were diluted by toluene with 1/40 weight ratio before analysis.

demonstrated as effective catalysts for PP degradation.⁶⁴ More recently, iron oxide-carbon composite catalysts have been produced which exhibit excellent catalytic performance in the thermal degradation of brominated acrylonitrile-butadiene-styrene (ABS)/PP blends.⁶⁵

To further characterize the polymer gel components, samples are collected and then subjected to thermogravimetric analysis (TGA) with a heating rate of $10\text{ }^\circ\text{C min}^{-1}$ in a nitrogen atmosphere, and the DTG curves are also presented in Fig. 4(a and b). The TGA curve of the as-received PP is also plotted for comparison. Obviously, the as-received PP shows the highest initial decomposition temperature (T_d), which starts from $\sim 400\text{ }^\circ\text{C}$ and completes at $475\text{ }^\circ\text{C}$. However, the collected polymer gel begins to lose weight at a much lower temperature ($\sim 50\text{ }^\circ\text{C}$) due to the existence of low-boiling-point small molecules. Comparing the TGA curves of SS(PP), SS3 and SS20,

it is interesting to observe that SS(PP) degrades more slowly than SS3 and SS20. Meanwhile, a sharp weight loss of 60% starting from $400\text{ }^\circ\text{C}$ and completing at $475\text{ }^\circ\text{C}$ is observed, which is highly consistent with the results from the as-received PP. The TGA curves for SS3 and SS20 are similar to each other and both of them follow a linear degradation pattern until a complete decomposition. The SS3 curve goes down even faster than SS20 especially below $350\text{ }^\circ\text{C}$, which is consistent with the GC-MS analysis that more low-boiling-point ($\text{C}_{13}\text{--}\text{C}_{19}$) components are obtained from SS3. The DTG curves for all the samples are plotted in Fig. 4(b). The major weight loss of PP and SS(PP) happens between 400 and $475\text{ }^\circ\text{C}$ with a sharp peak of large intensity in this region. On the contrary, the DTG curves for SS3 and SS20 were flattened and no such peaks were observed. These results indicate that the degradation of pure PP only generates small amount of light-weight components ($\sim 40\%$) and $\sim 60\%$ PP remains at its original molecular weight. With the addition of $\text{Fe@Fe}_2\text{O}_3$ NPs to the PP matrix, all the PP molecules have been decomposed and the amount of different carbon number species is evenly distributed as evinced by the flattened DTG curves. Moreover, it is worth mentioning that larger loadings of NPs do not contribute to a significant difference in the final polymer gel.

The formation mechanism for the dominant propylene oligomers ($\text{C}_{13=}$, $\text{C}_{19=}$, $\text{C}_{22=}$, *i.e.*, $\text{C}_{(3n+4)=}$, $n = 3, 4, 5, 6, \dots$) is illustrated in Scheme 3. Firstly, the reaction is initiated by the random scission of any PP chain to generate two shorter end-chain free radicals, as shown step (I) in Scheme 3. Secondly, the end-chain radicals can abstract hydrogen at different locations (such as a, b and c marked in Scheme 3) from a long PP chain to form a tertiary radical, step (II). Finally, the tertiary polymer radical is broken into two fragments undergoing a β -scission, one with a double bond at the end and the other with a secondary free radical, step (III).^{4,62}

3.3 Solid residue (SP3 and SP20)

3.3.1 Microstructure investigation. The solid residue after pyrolysis is collected and analyzed with high resolution TEM. Fig. 5(a) depicts the TEM microstructures of the SP3 NPs decomposed from S3 pyrolysis, which show a spherical nature with an average particle size of 11.0 nm (the inset column chart

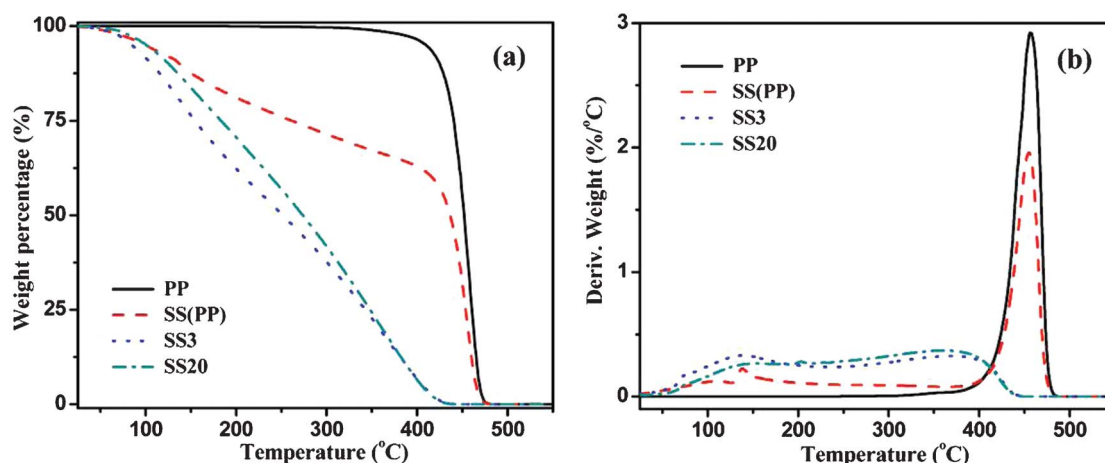
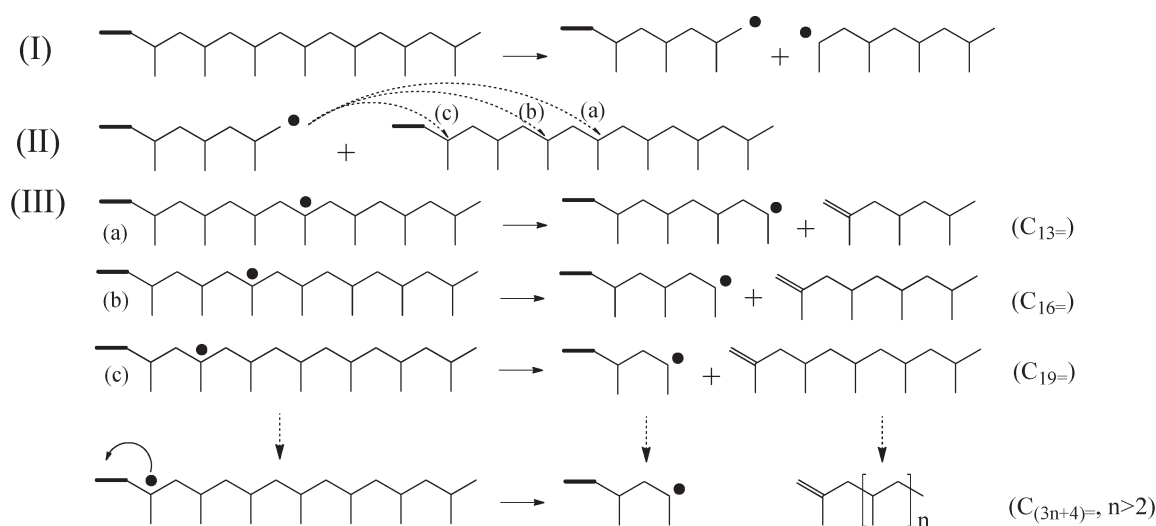


Fig. 4 (a) TGA curves for the PP and the polymer gel pyrolyzed from PP and NPs/PP PNCs in nitrogen, and (b) the corresponding DTG curves.



Scheme 3 The degradation mechanism for the polymer gels SS3/SS20.

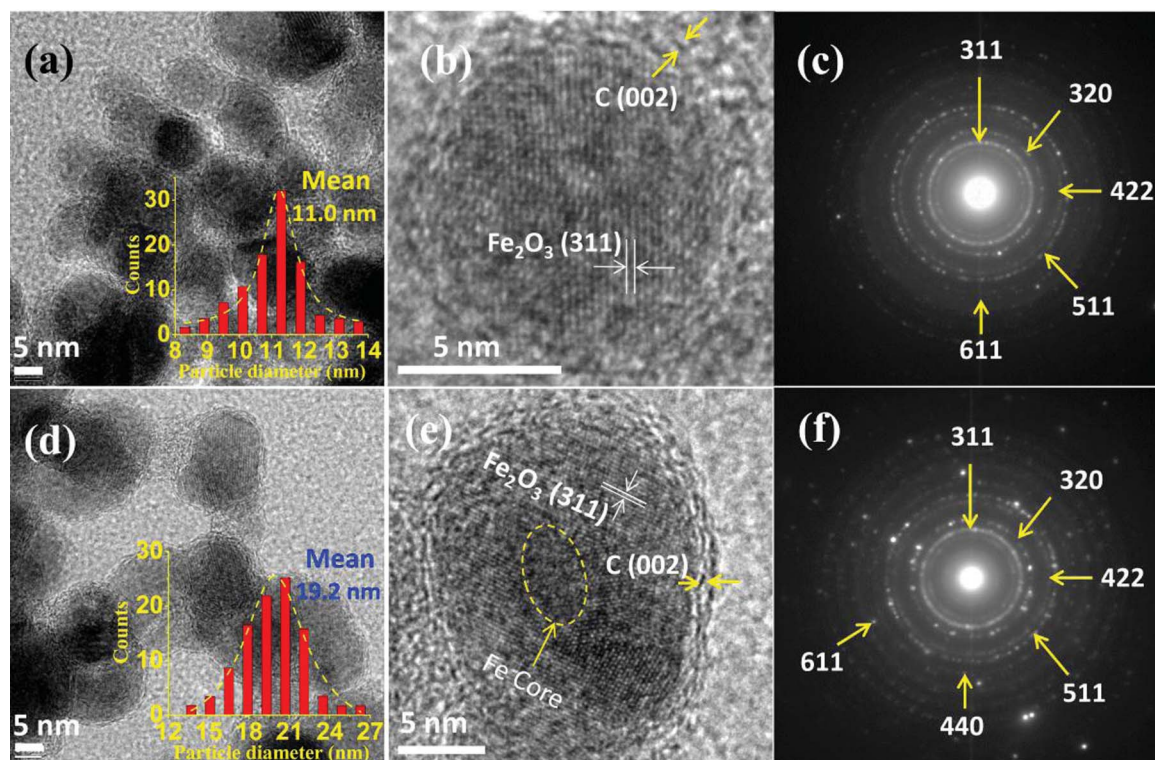


Fig. 5 (a) TEM, (b) HRTEM images and (c) selected area electron diffraction (SAED) of SP3 NPs; (d) TEM and (e) HRTEM and (f) SAED of SP20 NPs. Insets of (a) and (d) indicate the particle size distribution and mean value of the NPs.

of Fig. 5(a) shows the particle size distribution of SP3). All the NPs are wrapped with a thin layer of crystallized carbon shell, which could be clearly observed from the HRTEM, Fig. 5(b). The clear lattice fringe of the core indicates the crystal plane (311) of iron oxide (PDF#39-1346) and the lattice fringe of the graphite (002)⁶⁶ is clearly observed surrounding the NPs. During the thermal treatment, the attached polymer chains transform to carbon and finally the NPs are coated by the carbon shell. The selected area electron diffraction (SAED) pattern displayed in Fig. 5(c) indicates the crystalline planes of iron oxide (311),

(320), (422), (511) and (611) (PDF#39-1346). Fig. 5(d) shows the SP20 NPs decomposed from S20 with an average diameter of 19.2 nm (the inset column chart of Fig. 5(d) shows the particle size distribution of SP20), which is larger than that of the reported size of 15.9 ± 2.2 nm in Fe@Fe₂O₃/PP PNCs before thermal treatment.³¹ Both SP3 and SP20 shows relatively larger diameter than that of the NPs before annealing due to the carbon shell formation on the NP surface. The clear contrast difference in the HRTEM image in Fig. 5(e) indicates that the NPs are with a highly crystallized iron oxide core and the carbon shell is more

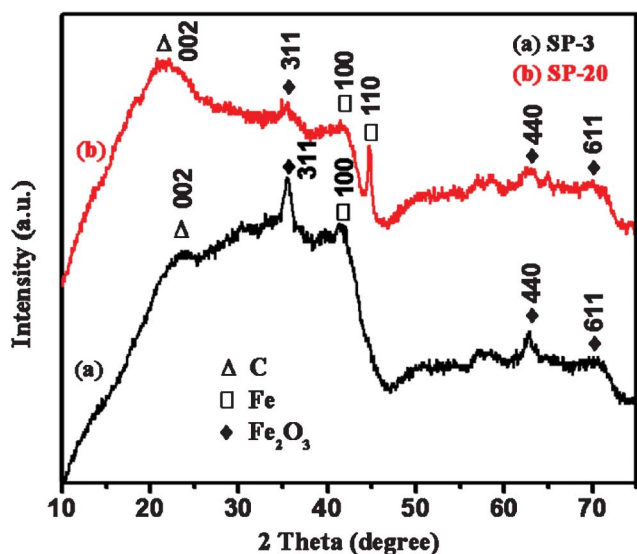


Fig. 6 XRD profiles of the solid residue from (a) 3.0 wt% NPs/PP, (b) 20.0 wt% NPs/PP.

compact than the one in Fig. 5(b). A similar SAED pattern of SP20 as compared to SP3 is observed with an additional crystalline plane of (440), Fig. 5(f). XRD patterns of the SP3/SP20 NPs are obtained in Fig. 6 to further identify the composition of the carbon-coated NPs. The broad peak near 25° is from graphitized carbon, which is more obvious in the SP20 NPs. The peaks at $2\theta = 42.27$ and 44.65° correspond to the (100) and (110) crystal planes of iron (PDF#06-0696) and other peaks at $2\theta = 35.80$, 62.45 , 71.20° are from the (311), (440) and (611) crystalline planes of iron oxide (PDF#39-1346). In contrast to the SP3 diffractogram, one more peak at 44.65° representing the iron (110) crystal plane is observed in the SP20 diffractogram. The undetectable signals of iron from HRTEM and SAED probably arise from the long time exposure of these particles to air before characterization which allows oxidation from iron to iron oxide.

3.3.2 Magnetic analysis. Fig. 7 shows the room temperature hysteresis loop of the SP3/SP20 NPs after pyrolysis. The very small coercivity (H_c , 2.3 Oe) reveals that the SP3 NPs are soft ferromagnets, while a significantly larger H_c is observed in SP20 NPs. The SP20 NPs exhibit much a higher saturated magnetization (M_s , 32.5 emu g^{-1}) than the SP3 NPs (6.0 emu g^{-1}). To acquire the magnetization of the iron-based core, thermogravimetric analysis (TGA), Fig. 8, is used to determine the specific weight fraction of the metal core and carbon shell within the magnetic carbon nanocomposites. Since the degradation of the carbon shell (or incompletely decomposed polymer species) is coupled with the oxidation of the metal core, the calculation for the weight fraction of each composition is difficult. The slight weight loss below 150°C is due to the evaporation of the moisture and after that both samples show a weight increase arising from the oxidation of the metal core. The TGA curve for the SP3 reaches the highest value at $\sim 238^\circ\text{C}$ followed by a sharp weight loss of about 15.8% owing to the decomposition of incompletely degraded polymer species and carbon (two degradation stages of SP3 in N_2 atmosphere are observed, which

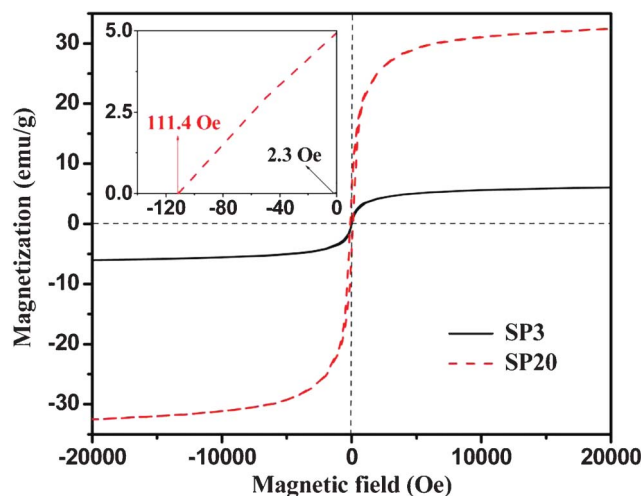


Fig. 7 Magnetic hysteresis loop of the SP3/SP20 NPs at room temperature. The inset shows the enlarged partial hysteresis loop.

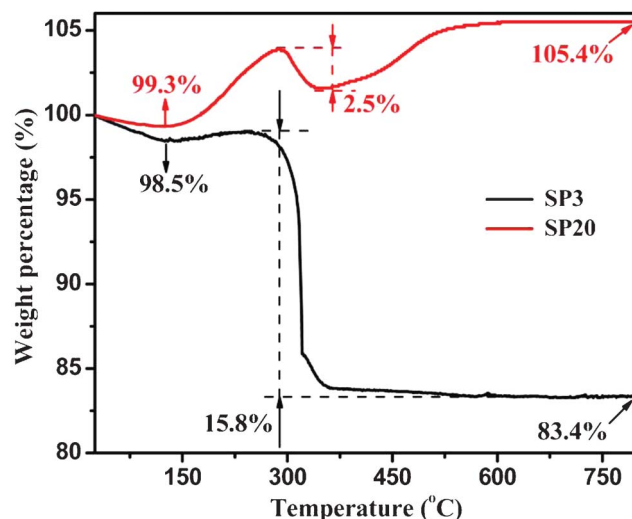


Fig. 8 Thermogravimetric curves of the SP3 and SP20 magnetic carbon nanocomposites.

show the DTG peak positions at $\sim 360^\circ\text{C}$ and $\sim 697^\circ\text{C}$ indicating the decomposition of polymer species and carbon, respectively). The PP has been completely decomposed in SP20 since only one degradation peak at 743°C is observed. Refer to Fig. S4†). The TGA curve for the SP20 goes up to the first peak point at $\sim 290^\circ\text{C}$ and experiences a 2.5% weight loss from carbon decomposition and continuously rises up to 105.4% at high temperatures. Based on the above observations, the carbon/residue polymer fraction in each sample is estimated to be $15.8 \pm 0.5\%$ and $2.5 \pm 1.0\%$ considering the oxidation induced weight increase during carbon decomposition. Therefore, the weight fraction of the iron/iron oxide core is calculated to be $84.2 \pm 0.5\%$ and $97.5 \pm 1.0\%$ for SP3 and SP20, respectively. The oxidation induced slight weight increase from 98.5% to 99.0% for SP3 indicates a negligible amount of iron in the core-shell NPs. The much larger weight increase of the SP20 reveals the higher fraction of pure iron, which is consistent with the XRD results in Fig. 6 and magnetic properties in Fig. 7. The

M_s of pure NPs within SP3 is calculated to be of 7.1 emu g^{-1} , which indicates a combination of the 2.7% pure iron and 97.3% $\alpha\text{-Fe}_2\text{O}_3$ (the M_s for bulk iron is 220.7 emu g^{-1} and $\alpha\text{-Fe}_2\text{O}_3$ is 1.2 emu g^{-1} at $10\,000 \text{ Oe}$ ⁶⁷). $\gamma\text{-Fe}_2\text{O}_3$ can be excluded since it has a much larger M_s of 64.0 emu g^{-1} .⁶⁸ The calculated M_s for the SP20 is 33.3 emu g^{-1} , indicating a larger fraction of 14.6% pure iron and 85.4% $\alpha\text{-Fe}_2\text{O}_3$.

3.4 Chromium removal

3.4.1 Effect of Cr(VI) and SP20 concentrations. The effect of initial Cr(VI) concentration on the removal efficiency of Cr(VI) at a solution pH (initial) of 7.0 using SP20 is shown in Fig. 9(a). The SP20 concentration was kept at a constant value of 1 g L^{-1} and a short contact time of 10 min was employed in this study. To evaluate the efficiency of SP20 for Cr(VI) removal from solution, removal percentage (RP, %) is introduced as a criterion which can be calculated using eqn (1).

$$\text{RP} = \frac{C_0 - C_r}{C_0} \times 100\% \quad (1)$$

where C_0 is the initial Cr(VI) concentration of the solution and C_r represents the remaining Cr(VI) existing in solution after the adsorption process. The linear relationship between Cr(VI) concentration and UV-vis absorption intensity at 540 nm is plotted in Fig. S5†. A maximum RP of about 99% was observed for an initial Cr(VI) concentration of 0.4 mg L^{-1} . Thereafter, the RP decreased with the increase of initial Cr(VI) concentration, Fig. 9(a). This is because the SP20 sites would eventually become saturated with adsorbed Cr(VI), at which point further addition of Cr(VI) to the solution hardly increase the amount of adsorbed Cr(VI) significantly. Keeping the highest Cr(VI) concentration of 1.5 mg L^{-1} with the same contact time of 10 min, different loadings of SP20 are applied to investigate the Cr(VI) RP, Fig. 9(b). It is observed that the RP increases almost linearly with the increase of SP20 loading due to the increased adsorption sites with larger amount of SP20 NPs. The maximum RP of 96.3% could be achieved at the SP20 loading of 2.5 g L^{-1} .

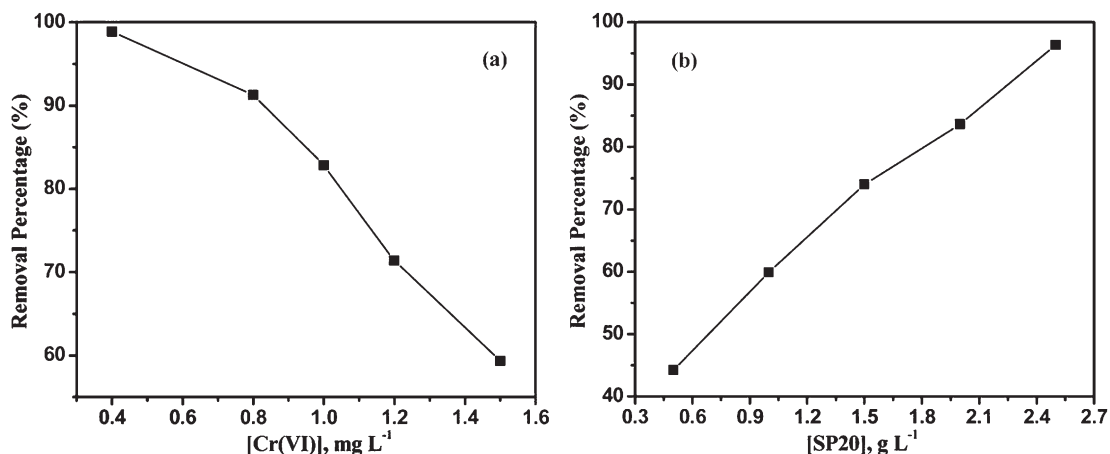


Fig. 9 Cr(VI) removal percentage (a) from Cr(VI) solution of different concentrations [SP20] = 1 g L^{-1} ; (b) with different SP20 concentrations, [Cr(VI)] = 1.5 mg L^{-1} . Adsorption time: 10 min. UV-vis spectra refer to ESI Fig. S6† and S7†.

3.4.2 Adsorption kinetics. The kinetics of the adsorption that describes the Cr(VI) uptake rate is one of the important characteristics, which controls the residence time of the adsorbate uptake at the solid–solution interface. Hence, in the present study, the kinetics of the Cr(VI) removal was carried out to understand the adsorption behavior of Cr(VI) on the SP20 NPs. Fig. 10 shows the adsorption data of Cr(VI) over SP20 at different time intervals (see Fig. S8† for the UV-vis spectra). Quantifying the changes in adsorption with time requires an appropriate kinetic model, and pseudo-first-order,⁶⁹ pseudo-second-order,⁷⁰ Elovich^{71,72} and intraparticle diffusion⁷³ kinetic models are investigated and compared. To evaluate the suitability of different models, the correlation coefficient (R^2 , close or equal to 1) is introduced. A higher R^2 value indicates a more applicable model to the kinetics of the Cr(VI) adsorption.

The fitting results obtained from different models are summarized in Table 2. With the highest correlation coefficient

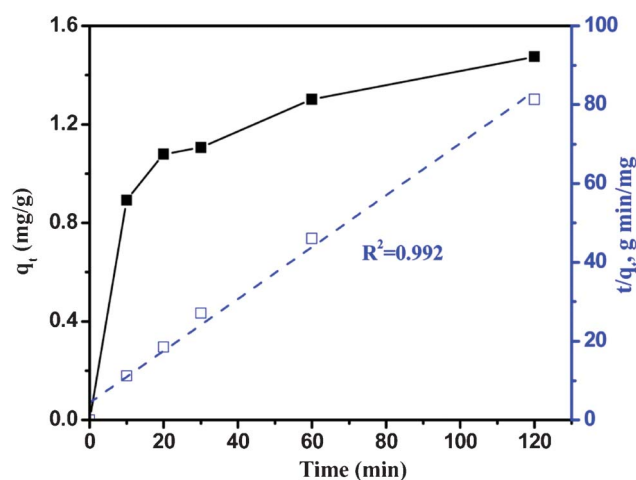


Fig. 10 Kinetic adsorption data plots of Cr(VI) by SP20: Cr(VI) removal rate q_t vs. time t (solid square) and the transformed rate plot t/q_t vs t (open square). [SP20] = 1 g L^{-1} , [Cr(VI)] = 1.5 mg L^{-1} , pH = 7. UV-vis spectra refer to ESI Fig. S8†.

Table 2 The parameters obtained from different kinetic models

Models	Equation ^a	Parameters	R ²
Pseudo-first-order ⁶⁹	$\log(q_e - q_t) = \log q_e - \frac{k_1}{2.303} t$	k_1 (min ⁻¹) 0.089	0.953
Pseudo-second-order ⁷⁰	$\frac{t}{q_t} = \frac{1}{k_{ad} q_e^2} + \frac{t}{q_e}$	k_{ad} (g mg ⁻¹ min ⁻¹) 0.099	0.992
Elovich ^{71,72}	$q_t = \frac{I}{\beta} \ln(\alpha\beta) + \frac{I}{\beta} \ln(t)$	α (mg g ⁻¹ min ⁻¹) 1.102	0.976
Intraparticle diffusion ⁷³	$q_t = k_{dif} t^{0.5} + C$	k_{dif} (mg g ⁻¹ min ^{-0.5}) 0.073	0.936

^a q_t is the solid-phase loading of Cr(VI) in the adsorbent at time t , q_e is the adsorption capacity at equilibrium, k_1 is the rate constant of pseudo-first-order adsorption. In pseudo-second-order model, k_{ad} is the rate constant of adsorption and h is the initial adsorption rate at t approaching zero, $h = k_{ad} q_e^2$. α and β represent the initial adsorption rate and desorption constant in the Elovich model. k_{dif} indicates the intraparticle diffusion rate constant and C provides information about the thickness of the boundary layer.

of $R^2 = 0.992$ (fitting curve is shown in Fig. 10, open square curve), the pseudo-second-order model provides an excellent correlation for the adsorption of Cr(VI) on SP20. The R^2 for the pseudo-first-order, Elovich and intraparticle diffusion models are 0.953, 0.976 and 0.936, respectively, indicating that these models are less suitable than that of the pseudo-second-order model for describing the Cr(VI) adsorption on SP20. The higher adsorption rate constant k_{ad} (0.099 g mg⁻¹ min⁻¹) of SP20 from the pseudo-second-order model than that of aluminum magnesium mixed hydroxide (<0.024 g mg⁻¹ min⁻¹),⁷⁴ pomegranate husk carbon (<0.032 g mg⁻¹ min⁻¹)⁷⁵ and activated carbon (<0.093 g mg⁻¹ min⁻¹)⁷⁶ indicates the much faster removal rate with SP20.

3.4.3 pH effect. Solution pH is one of the most important variables affecting the adsorption characteristics. The Cr(VI) removal efficiency by SP20 in different pH solutions is shown in Fig. 11 with an initial Cr(VI) concentration of 1.5 mg L⁻¹ and SP20 concentration of 1 g L⁻¹ (see Fig. S9† for the UV-vis spectra). At a fixed adsorbent concentration, complete Cr(VI) removal was achieved under acidic conditions when the pH is between 1 to 3 rather than in neutral and basic conditions. By increasing solution pH to 5 and even higher, the RP decreases significantly. Within the solution at pH = 11, only 5% RP is observed. It is worthwhile to mention that SP20 is relatively

difficult to separate from the liquid suspension by centrifuge after adsorption in solutions with the pH equal to 1 and 2, which can probably be attributed to the etching effect of the protons in the acidic solution on the iron oxide core. After the core has been etched off, only light weight carbon shell exists in the solution and thus these materials are difficult to separate. Cr(VI) exists with different ionic forms in solution. The most important ion forms in solution are chromate (CrO₄²⁻), dichromate (Cr₂O₇²⁻) and hydrogen chromate (HCrO₄⁻) and these ion forms are related to the solution pH and total chromate concentration.^{74,77} The predominance diagram⁷⁴ of the chromium species based on the thermodynamic database^{78,79} using both pH and total Cr(VI) as variables indicates that the major species of Cr(VI) are CrO₄²⁻ and HCrO₄⁻. For pHs lower than 6.8, HCrO₄⁻ is the dominant species and above 6.8 only CrO₄²⁻ is stable. The results show that SP20 nanocomposites favor the adsorption of HCrO₄⁻ rather than CrO₄²⁻. The dependence of the Cr(VI) removal on the solution pH can be explained from the perspective of the surface chemistry at the interface. With an increase in pH, the uptake of the Cr(VI) ions decreases, which is due to the higher concentration of the OH⁻ ions present in the mixture that compete with Cr(VI) species on the SP20 NPs.

4. Conclusion

To recycle magnetic Fe@Fe₂O₃/PP polymer nanocomposites (PNCs) into useful chemical species and valuable magnetic carbon nanocomposites (MCNCs) in a sustainable way has been achieved with a looped carbon capturing feature. The Fe@Fe₂O₃ NPs within the PNCs (even in small amounts, for example, 3 wt%) play a significant role in the degradation of the PP matrix due to their catalytic activity. The decomposed species of the volatile components are almost the same for pure PP and PNCs but the major species such as 2,5-dimethyl-3-hexene, 3,4-diethyl-3-hexene, 3-methyl-1-butene and 1-pentene are in different fractions. The condensed polymer gel components decomposed from PNCs obtain a much higher fraction of light-weight species, for example, the concentration of the C₁₃-C₄₃ species is almost doubled as compared to the same species from pure PP. In addition, TGA results reveal that only 40% of the PP is degraded to lower molecular weight species following the same pyrolysis process from pure PP without NPs. The conventional coked solid residue is utilized as a carbon source to *in situ* synthesize carbon-coated NPs. The carbon-coated magnetic nanocomposites

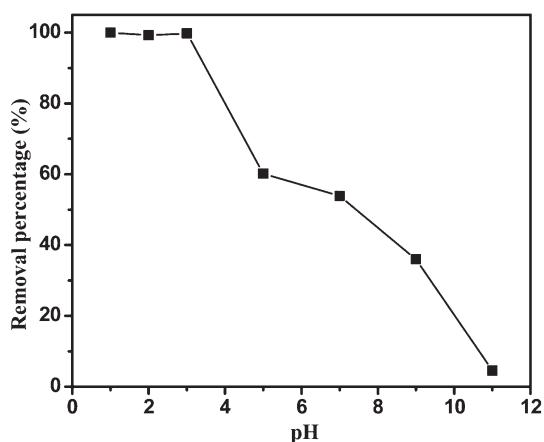


Fig. 11 The effect of solution pH on Cr(VI) removal efficiency of SP20. [SP20] = 1 g L⁻¹, [Cr(VI)] = 1.5 mg L⁻¹, treating time: 10 min. For UV-vis spectra refer to ESI Fig. S9†.

pyrolyzed from PNCs containing 20.0 wt% NPs show high adsorption capacity (1.5 mg g⁻¹) and fast Cr(VI) removal from waste water. Typically, a 99% Cr(VI) removal percentage can be achieved within 10 min and the Cr(VI) concentration could be controlled well below the EPA regulation of 100 µg L⁻¹. Kinetic investigation reveals a pseudo-second-order adsorption of Cr(VI) on the synthesized MCNCs. These MCNCs present higher adsorption capacity at lower pH solutions and the strong magnetization facilitates their easy separation from solution using a permanent magnet, which is an energetically and economically sustainable process.

Acknowledgements

This project is financially supported by the National Science Foundation—Chemical and Biological Separations (EAGER: CBET 11-37441) managed by Dr Rosemarie D. Wesson. We acknowledge the support from the National Science Foundation—Nanoscale Interdisciplinary Research Team and Materials Processing and Manufacturing (CMMI 10-30755) managed by Dr Mary M. Toney to obtain the DSC and TGA equipments. D. P. Young acknowledges support from the NSF under Grant No. DMR 10-05764.

References

- X. Qi, G. Poernomo, K. Wang, Y. Chen, M. B. Chan-Park, R. Xu and M. W. Chang, *Nanoscale*, 2011, **3**, 1874–1880.
- R. S. Stein, *Proc. Natl. Acad. Sci. U. S. A.*, 1992, **89**, 835–838.
- S. Kobayashi, H. Uyama and T. Takamoto, *Biomacromolecules*, 2000, **1**, 3–5.
- T. M. Kruse, H. -W. Wong and L. J. Broadbelt, *Macromolecules*, 2003, **36**, 9594–9607.
- G. Manos, A. Garforth and J. Dwyer, *Ind. Eng. Chem. Res.*, 2000, **39**, 1203–1208.
- G. de la Puente and U. Sedran, *Appl. Catal., B*, 1998, **19**, 305–311.
- J.-S. Kim, W.-Y. Lee, S.-B. Lee, S.-B. Kim and M.-J. Choi, *Catal. Today*, 2003, **87**, 59–68.
- K. Gobin and G. Manos, *Polym. Degrad. Stab.*, 2004, **86**, 225–231.
- J. Zhu, S. Wei, J. Ryu, L. Sun, Z. Luo and Z. Guo, *ACS Appl. Mater. Interfaces*, 2010, **2**, 2100–2107.
- J. Zhu, S. Wei, M. Alexander Jr., T. D. Dang, T. C. Ho and Z. Guo, *Adv. Funct. Mater.*, 2010, **20**, 3076–3084.
- J. Zhu, S. Wei, J. Ryu, M. Budhathoki, G. Liang and Z. Guo, *J. Mater. Chem.*, 2010, **20**, 4937–4948.
- P. Mavinakuli, S. Wei, Q. Wang, A. B. Karki, S. Dhage, Z. Wang, D. P. Young and Z. Guo, *J. Phys. Chem. C*, 2010, **114**, 3874–3882.
- J. Zhu, S. Wei, A. Yadav and Z. Guo, *Polymer*, 2010, **51**, 2643–2651.
- J. Zhu, S. Wei, L. Zhang, Y. Mao, J. Ryu, P. Mavinakuli, A. B. Karki, D. P. Young and Z. Guo, *J. Phys. Chem. C*, 2010, **114**, 16335–16342.
- J. Zhu, S. Wei, L. Zhang, Y. Mao, J. Ryu, A. B. Karki, D. P. Young and Z. Guo, *J. Mater. Chem.*, 2011, **21**, 342–348.
- J. Zhu, S. Wei, L. Zhang, Y. Mao, J. Ryu, N. Haldolaarachchige, D. P. Young and Z. Guo, *J. Mater. Chem.*, 2011, **21**, 3952–3959.
- J. Zhu, S. Wei, R. Patil, D. Rutman, A. S. Kucknoor, A. Wang and Z. Guo, *Polymer*, 2011, **52**, 1954–1962.
- H. Wei, X. Yan, Y. Li, S. Wu, A. Wang, S. Wei and Z. Guo, *J. Phys. Chem. C*, 2012, **116**, 4500–4510.
- P. Kim, N. M. Doss, J. P. Tillotson, P. J. Hotchkiss, M. -J. Pan, S. R. Marder, J. Li, J. P. Calame and J. W. Perry, *ACS Nano*, 2009, **3**, 2581–2592.
- J. Zang and X. Li, *J. Mater. Chem.*, 2011, **21**, 10965–10969.
- P. Vacca, G. Nenna, R. Miscioscia, D. Palumbo, C. Minarini and D. D. Sala, *J. Phys. Chem. C*, 2009, **113**, 5777–5783.
- K. Ding, H. Jia, S. Wei and Z. Guo, *Ind. Eng. Chem. Res.*, 2011, **50**, 7077–7082.
- J. Zhu, S. Wei, J. Ryu and Z. Guo, *J. Phys. Chem. C*, 2011, **115**, 13215–13222.
- Z. Guo, S. Park, H. T. Hahn, S. Wei, M. Moldovan, A. B. Karki and D. P. Young, *J. Appl. Phys.*, 2007, **101**, 09M511.
- J. Zhu, S. Wei, N. Haldolaarachchige, D. P. Young and Z. Guo, *J. Phys. Chem. C*, 2011, **115**, 15304–15310.
- G. L. Bezemer, J. H. Bitter, H. P. C. E. Kuipers, H. Oosterbeek, J. E. Holewijn, X. Xu, F. Kapteijn, A. J. van Dillen and K. P. de Jong, *J. Am. Chem. Soc.*, 2006, **128**, 3956–3964.
- A. Chambers, T. Nemes, N. M. Rodriguez and R. T. K. Baker, *J. Phys. Chem. B*, 1998, **102**, 2251–2258.
- J. Zhu, S. Wei, Y. Li, S. Pallavkar, H. Lin, N. Haldolaarachchige, Z. Luo, D. P. Young and Z. Guo, *J. Mater. Chem.*, 2011, **21**, 16239–16246.
- P. Gambardella, S. Rusponi, M. Veronese, S. S. Dhese, C. Grazioli, A. Dallmeyer, I. Cabria, R. Zeller, P. H. Dederichs, K. Kern, C. Carbone and H. Brune, *Science*, 2003, **300**, 1130–1133.
- W. Z. Li, S. S. Xie, L. X. Qian, B. H. Chang, B. S. Zou, W. Y. Zhou, R. A. Zhao and G. Wang, *Science*, 1996, **274**, 1701–1703.
- J. Zhu, S. Wei, Y. Li, L. Sun, N. Haldolaarachchige, D. P. Young, C. Southworth, A. Khasanov, Z. Luo and Z. Guo, *Macromolecules*, 2011, **44**, 4382–4391.
- Z. Guo, S. Park, H. T. Hahn, S. Wei, M. Moldovan, A. B. Karki and D. P. Young, *Appl. Phys. Lett.*, 2007, **90**, 053111.
- Z. Guo, C. S. R. Kumar, L. L. Henry, E. E. Doomes, J. Hormes and E. J. Podlaha, *J. Electrochem. Soc.*, 2005, **152**, D1–D5.
- J. Zhu, S. Wei, X. Chen, A. B. Karki, D. Rutman, D. P. Young and Z. Guo, *J. Phys. Chem. C*, 2010, **114**, 8844–8850.
- X. Chen, S. Wei, C. Gunesoglu, J. Zhu, C. S. Southworth, L. Sun, A. B. Karki, D. P. Young and Z. Guo, *Macromol. Chem. Phys.*, 2010, **211**, 1775–1783.
- J. Zhu, S. Wei, D. Rutman, N. Haldolaarachchige, D. P. Young and Z. Guo, *Polymer*, 2011, **52**, 2947–2955.
- S. Wei, R. Patil, L. Sun, N. Haldolaarachchige, X. Chen, D. P. Young and Z. Guo, *Macromol. Mater. Eng.*, 2011, **296**, 850–857.
- Z. Guo, H. T. Hahn, H. Lin, A. B. Karki and D. P. Young, *J. Appl. Phys.*, 2008, **104**, 014314.
- N. J. Tang, W. Chen, W. Zhong, H. Y. Jiang, S. L. Huang and Y. W. Du, *Carbon*, 2006, **44**, 423–427.
- D. Zhang, R. Chung, A. B. Karki, F. Li, D. P. Young and Z. Guo, *J. Phys. Chem. C*, 2010, **114**, 212–219.
- S. Wei, Q. Wang, J. Zhu, L. Sun, H. Lin and Z. Guo, *Nanoscale*, 2011, **3**, 4474.
- J. Zhu, S. Wei, I. Y. Lee, S. Park, J. Willis, N. Haldolaarachchige, D. P. Young and Z. Guo, *RSC Adv.*, 2012, **2**, 1136.
- J. L. Wilson, P. Poddar, N. A. Frey, H. Srikanth, K. Mohamed, J. P. Harmon, S. Kotha and J. Wachsmuth, *J. Appl. Phys.*, 2004, **95**, 1439–1443.
- S. R. Rudge, T. L. Kurtz, C. R. Vessely, L. G. Catterall and D. L. Williamson, *Biomaterials*, 2000, **21**, 1411–1420.
- D. Zhang, S. Wei, C. Kaila, X. Su, J. Wu, A. B. Karki, D. P. Young and Z. Guo, *Nanoscale*, 2010, **2**, 917–919.
- Z. Guo, M. Moldovan, D. P. Young, L. L. Henry and E. J. Podlaha, *Electrochem. Solid-State Lett.*, 2007, **10**, E31–E35.
- Z. Lu, M. D. Prouty, Z. Guo, V. O. Golub, C. S. S. R. Kumar and Y. M. Lvov, *Langmuir*, 2005, **21**, 2042–2050.
- J. Hassoun, G. Derrien, S. Panero and B. Scrosati, *Adv. Mater.*, 2008, **20**, 3169.
- T. Hayashi, S. Hirono, M. Tomita and S. Umemura, *Nature*, 1996, **381**, 772–774.
- P. J. F. Harris and S. C. Tsang, *Chem. Phys. Lett.*, 1998, **293**, 53–58.
- T. Yamada, T. Namai, K. Hata, D. N. Futaba, K. Mizuno, J. Fan, M. Yudasaka, M. Yumura and S. Iijima, *Nat. Nanotechnol.*, 2006, **1**, 131–136.
- J. Zhu, S. Wei, H. Gu, S. B. Rapole, Q. Wang, Z. Luo, N. Haldolaarachchige, D. P. Young and Z. Guo, *Environ. Sci. Technol.*, 2012, **46**, 977.
- F. Ding, A. Rosén, E. E. B. Campbell, L. K. L. Falk and K. Bolton, *J. Phys. Chem. B*, 2006, **110**, 7666–7670.
- D. Mohan and C. U. Pittman Jr, *J. Hazard. Mater.*, 2006, **137**, 762–811.
- C. P. Huang and M. H. Wu, *Water Res.*, 1977, **11**, 673–679.
- D. Park, Y. -S. Yun, J. Hye Jo and J. M. Park, *Water Res.*, 2005, **39**, 533–540.
- C. Namasivayam and K. Ranganathan, *Environ. Pollut.*, 1993, **82**, 255–261.
- M. Zhu and G. Diao, *Nanoscale*, 2011, **3**, 2748–2767.

- 59 T. W. Smith and D. Wychick, *J. Phys. Chem.*, 1980, **84**, 1621–1629.
- 60 J. V. Wouterghem, S. Mørup, S. W. Charles, S. Wells and J. Villadsen, *Phys. Rev. Lett.*, 1985, **55**, 410.
- 61 M. Gardner and S. Comber, *Analyst*, 2002, **127**, 153–156.
- 62 H.-W. Wong and L. J. Broadbelt, *Ind. Eng. Chem. Res.*, 2001, **40**, 4716–4723.
- 63 Y. Tsuchiya and K. Sumi, *J. Polym. Sci., Part A-1*, 1969, **7**, 1599.
- 64 M. Day, J. D. Cooney and M. MacKinnon, *Polym. Degrad. Stab.*, 1995, **48**, 341–349.
- 65 T. Bhaskar, K. Murai, M. Brebu, T. Matsui, M. A. Uddin, A. Muto and Y. Sakata, *Green Chem.*, 2002, **4**, 603–606.
- 66 S. H. Park, S. M. Jo, D. Y. Kim, W. S. Lee and B. C. Kim, *Synth. Met.*, 2005, **150**, 265–270.
- 67 X.-M. Liu, S.-Y. Fu, H.-M. Xiao and C.-J. Huang, *J. Solid State Chem.*, 2005, **178**, 2798–2803.
- 68 B. R. V. Narasimhan, S. Prabhakar, P. Manohar and F. D. Gnanam, *Mater. Lett.*, 2002, **52**, 295–300.
- 69 S. Lagergren, Zur theorie der sogenannten adsorption gelöster stoffe, Kungliga Svenska Vetenskapsakademiens, *Handlingar*, 1898, **24**, 1–39.
- 70 Y. S. Ho, G. McKay, D. A. J. Wase and C. F. Forster, *Adsorpt. Sci. Technol.*, 2000, **18**, 639–650.
- 71 R. -S. Juang and M. -L. Chen, *Ind. Eng. Chem. Res.*, 1997, **36**, 813–820.
- 72 D. L. Sparks, ed., *Kinetics of Reaction in Pure and Mixed Systems, in Soil Physical Chemistry*, CRC press, Boca Raton, 1986.
- 73 S. K. Srivastava, R. Tyagi and N. Pant, *Water Res.*, 1989, **23**, 1161–1165.
- 74 Y. Li, B. Gao, T. Wu, D. Sun, X. Li, B. Wang and F. Lu, *Water Res.*, 2009, **43**, 3067–3075.
- 75 N. Ahmed El, *J. Hazard. Mater.*, 2009, **161**, 132–141.
- 76 A. El-Sikaily, A. E. Nemr, A. Khaled and O. Abdelwehab, *J. Hazard. Mater.*, 2007, **148**, 216–228.
- 77 B. M. Weckhuysen and I. E. Wachs, *Chem. Rev.*, 1996, **96**, 3327–3349.
- 78 J. N. Butler, *Ionic Equilibrium*, 1967, Addison-Wesley, New York.
- 79 W. Stumm and J. J. Morgan, *Aquatic Chemistry: An Introduction Emphasizing Chemical Equilibria in Natural Waters*, 1996, John Wiley & Sons, Inc., New York.